https://doi.org/10.1016/j.compositesa.2023.107522

Anisotropic Thermally Superinsulating Boron Nitride Composite Aerogel for Building Thermal Management

Miracle Hope Adegun[1], Kit-Ying Chan[2], Jie Yang[1], Harun Venkatesan[1], Eunyoung Kim[1], Heng Zhang[1], Xi Shen[2,3,*], Jinglei Yang[1], Jang-Kyo Kim[1,4,*]

[1] Department of Mechanical and Aerospace Engineering, The Hong Kong University of Science and Technology, Clearwater Bay, Kowloon, Hong Kong

[2] Department of Aeronautical and Aviation Engineering, The Hong Kong Polytechnic University, Hung Hom, Kowloon, Hong Kong

[3] The Research Institute for Sports Science and Technology, The Hong Kong Polytechnic University, Hung Hom, Kowloon, Hong Kong

[4] School of Mechanical and Manufacturing Engineering, The University of New South Wales, Sydney, NSW 2052, Australia

Corresponding authors: Xi Shen (xi.shen@polyu.edu.hk); Jang-Kyo Kim (mejkkim@ust.hk)

Keywords: Boron nitride nanosheets, aerogel, freeze-casting, thermal insulation

Highlights:

- Lightweight composite aerogels with aligned porous channels are fabricated using environmentally friendly materials based on the unidirectional freeze-casting process.
- The aerogels deliver a combination of ultralow thermal conductivity, high solar-weighted reflectance and high thermal emittance within the atmospheric window, making them ideal for thermal insulation in buildings.
- The high solar reflectance of 95 % over the whole sunlight wavelength of 0.3 – 2.5 μm and near unity emittance above 93 % in the atmospheric window range of 8 – 13 μm enable the composite aerogel to maintain the normal body temperature even under the high solar irradiance.
- The aerogel is able to maintain about 50 % reduction in cooling energy consumption of a building model.

TOC

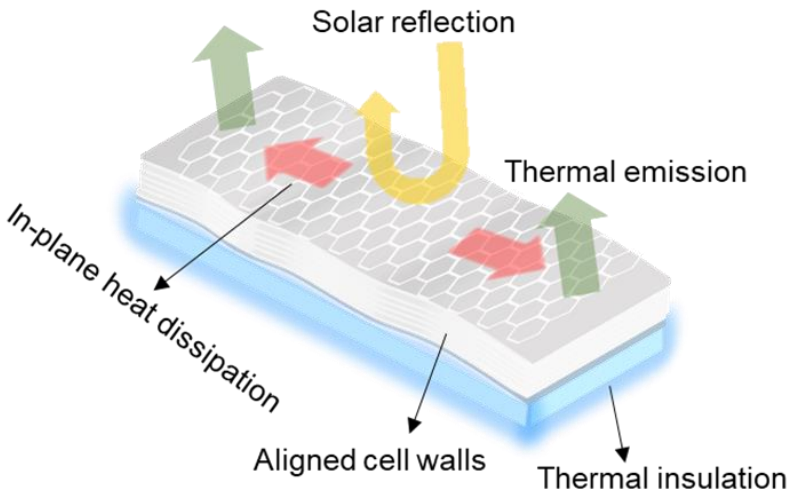

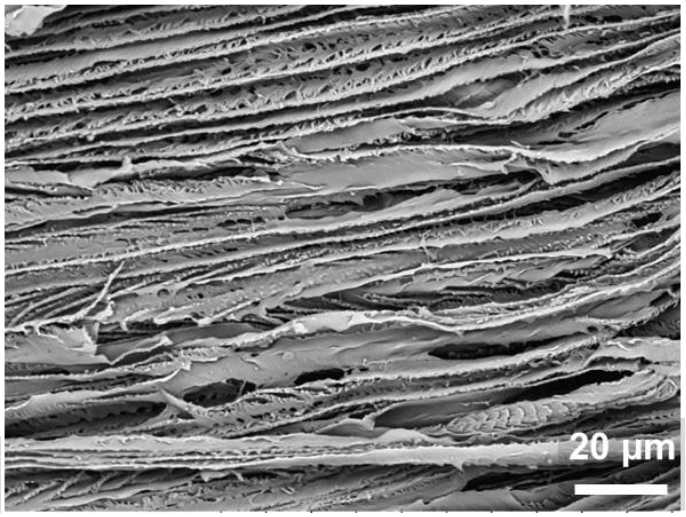

An anisotropic and lightweight BNNS/PVA composite aerogel is rationally designed using the unidirectional freeze-casting technique. The composite aerogel with optimal BNNS and PVA loadings possesses highly aligned porous channels delivering a combination of ultralow thermal conductivity, very high solar reflectance and thermal emittance in the atmospheric transparency windows. This desired trait makes the composite aerogel a promising candidate for thermal management in buildings and other applications requiring efficient thermal insulation.

Abstract

Thermally insulating materials are commonly used to reduce energy consumption in buildings. Most commercial products possess only low thermal conductivities but poor insulating capabilities in the daytime with little sunlight reflectance and thermal emittance. It is challenging to achieve all traits in the same material. Herein, anisotropic boron nitride nanosheet (BNNS)/polyvinyl alcohol composite aerogels are developed using the unidirectional freeze-casting technique. Benefitting from the aligned porous structure, the composite aerogel with an optimal BNNS content exhibits a combination of an ultralow TC of 20.3 mW/mK in the through-thickness direction, a high solar-weighted reflectance of 95.0 % over the whole sunlight wavelength and a high emittance of above 93 % within the atmospheric transparency window. These exceptional thermo-optical properties enable the composite aerogel to maintain the interior temperature much cooler than commercially available foams, making them promising candidates as superinsulating envelopes for energy saving in buildings towards carbon neutrality.

1. Introduction

The conventional method of maintaining interior thermal comfort requires expending a large amount of energy. It has been estimated that more than 10 % of the global energy is consumed to maintain human thermal comfort [1,2]. Further, the air conditioners used to achieve a pleasant interior temperature inevitably emit greenhouse gases which constitute environmental pollution contributing to global warming [3,4]. It was estimated that building energy consumption account for 30 % of carbon dioxide emission, which is a big threat to the environment [5–7]. In order to mitigate this, it becomes necessary to develop thermally insulating materials that utilize zero energy consumption [8].

Currently, indoor thermal comfort has been realized by constructing building envelopes with thermally insulating properties. These insulating structures are made by utilizing either materials with low thermal conductivities (TCs) that can reduce the heat exchange between the exterior and interior of a building or highly reflective coatings that can minimize heat absorbed from sunlight into the building [9–11]. Mineral wool, wood fibers, fiberglass, polypropylene nonwoven fabrics, porous aramid fibers and commercially available thermal insulating foams such as expanded

polystyrene (EPS) and polyurethane (PU) foam are the conventional materials used for thermal insulation [8,12–15]. However, they exhibit TCs higher than that of air (24 mW/mK), thereby limiting their insulation performance. Three-dimensional (3D) porous aerogels are envisaged as potential insulating materials due to their low densities and high porosities [16–18]. Commonly fabricated among them are ceramic-based and polymer-based aerogels. On one hand, ceramic aerogels made from silica (SiO_2), silicon carbide (SiC), [19,20] and boron nitride (BN) [21–24] show a good promise given their low TCs of ~ 20 mW/mK, but they have major drawbacks arising from the complex fabrication process, mechanical brittleness, and high cost [25–27]. On the other hand, polymer aerogels have higher ductility than silica-based counterparts but their TCs are usually higher than that of air [28].

To reconcile the above trade-off between thermal insulation and mechanical properties, the respective advantageous characteristics of ceramic and polymer aerogels have been exploited to develop ceramic/polymer composite aerogels with various pore structures [14,29,30]. The efficiency of thermal insulation is often influenced by the rate of heat dissipation which in turn is dependent on the composite pore structure. Isotropic porous structures are disadvantageous by heat localization which adversely affects the overall thermal performance [11,31] . Anisotropic porous structures, in contrast, can achieve thermal insulation in the transverse direction ($TC_{\perp}$) and heat dissipation in the axial direction (TC_L) of pore alignment, thereby preventing the build-up of heat within the material and enhancing thermal insulation [11,14,31,32]. The difference in thermal conductivities in the anisotropic structure is described by the TC anisotropy ratio ($TCAR = {TC_L}/{TC_{\perp}}$), which can be increased by incorporating anisotropic nanofillers into the matrix [30]. The anisotropic nanofillers, such as BN nanosheets (BNNS) and graphene, can improve the TC_L of composite aerogels by leveraging their high in-plane TCs without significantly increasing the $TC_{\perp}$ thanks to their much inferior through-the-thickness TCs [30]. Further modifying the pore walls with nanoscale constituents creates interfacial thermal resistance serving as the barrier to phonon transport, which minimizes the solid heat conduction and overall TC [14], imparting an ultralow $TC_{\perp}$ of only 15 mW/mK.

In addition to ultralow TCs, thermally insulating materials should also present a good solar reflectance characteristic so as to reduce the heat absorbed from sunlight into the building during daytime. Solar-reflective coatings consisting of light-scattering dielectric fillers such as silicon

dioxide have been applied on the surface of thermally insulating aerogels to reflect solar radiation [9,10] . Nonetheless, the solar reflectance of these coatings is often limited by the low refractive indices (n = 1.46 – 1.65) of the above dielectric fillers, which have little contrast with those of polymer matrix (n = 1.3 – 1.7) to generate effective interfacial light scattering [33]. Moreover, the coatings inevitably increase the TCs of the underlying aerogels because of the relatively high TCs of dielectric particles in the coatings. Instead of using dielectric fillers, recent efforts have focused on introducing pores as light scatterers to achieve a high solar reflectance of over 90 % in porous films or aerogels by exploiting the refractive index mismatch between air (n = 1) and polymer-based pore walls (n = 1.3 – 1.7). Although the presence of pores is also helpful in reducing the TC, it is still difficult to achieve thermal superinsulation (*i.e.*, with TC less than air) in solar-reflective aerogels due to the lack of rational design of the pore wall compositions and structures. For instance, an anisotropic thermally insulating nanowood with a high solar reflectance of 95 % exhibited a TC of 30 mW/mK in the transverse direction [34] while a cooling wood with a high solar reflectance of 96 % had a high TC of 185 mW/mK [35]. Other examples also include an isotropic thermally insulating polyethylene aerogel (PEA) with a high reflectance of 92.2 % and a TC of 28 mW/mK [36] as well as a cooling skin fabricated by laminating polydimethylsiloxane film with PEA exhibiting a high solar reflectance of ~96 % and a TC of 32 mW/mK [37]. The foregoing examples signify that achieving a high solar reflectance with an ultralow TC is still a challenge. Furthermore, high long-wave infrared (LWIR) emissivity in the atmospheric transparency window ranging from 8 to 13 μm is also highly desired so that the heat absorbed from the sun can be radiated back to the cold space, leading to passive cooling with zero energy consumption [38]. To achieve a sub-ambient cooling effect, the solar reflectance is estimated to be at least 94 %, entailing a complex structural design consisting of additional thermal emitter covered with reflective foils [37,39]. It is therefore imperative to develop thermally insulating materials with low TCs to minimize heat exchange from outdoor to indoor along with simultaneously high solar reflectances and high thermal emittances to reduce the heat generated by solar absorption. This requires a bottom-up approach involving a synergy between the fabrication method and the choice of fillers.

In this work, a unidirectional freeze-casting (UFC) technique was used to fabricate anisotropic BNNS/polyvinyl alcohol (PVA) composite aerogels. Two-dimensional (2D) BNNS is a promising filler to achieve the required thermo-optical properties because of its anisotropic properties

including a high TC of 360 W/mK along the basal plane and a low TC of 2 W/mK in the thickness direction [40–42]. By aligning BNNS along the cell walls using the freeze-casting technique, a low solid thermal conduction is expected in the thickness direction of the cell walls. In addition, unlike the open-pore structures formed by the interconnected isotropic nanoparticles in conventional SiO_2 or Al_2O_3-based aerogels, the 2D BNNS can divide the aerogel into isolated cells, effectively reducing the air conduction and convection for achieving an ultralow thermal conductivity [24]. Moreover, the BNNS also has a large refractive index of 2.1, which is much higher than conventional SiO_2 (~1.47) and Al_2O_3 (~1.77) nanoparticles [33]. The much-different refractive index of BNNS from that of the polymer matrix (~1.5) imparts effective scattering of incident light at the BNNS/matrix interfaces for a high solar reflectance [41]. These anisotropic features of BNNS were tailored to yield thermally superinsulating materials with excellent solar reflectance. The lightweight composites consist of elongated pores between highly-aligned cell walls created by the UFC process, endowing the aerogels with an ultralow TC of 20.3 mW/mK in the through-thickness direction. The porous aerogel structure also presents an excellent solar-weighted reflectance of 95.0 % over the whole sunlight wavelength of 0.3 – 2.5 μm as well as an emittance of 93 % within the atmospheric window of 8 – 13 μm. The excellent thermal insulation and wavelength-dependent optical responses enable the composite aerogels to maintain an internal temperature close to the normal body temperature of 37 °C under the high solar irradiance, 12 °C lower than the temperature recorded by of commercial EPS foam under the same condition. These desired characteristics make them promising materials for passive thermal management in buildings and thermo-protective covers as well as other applications requiring protection from high solar irradiance.

2. Experimental Methods

2.1 Materials and Fabrication of BNNS/PVA Aerogel

The UFC process used for the fabrication of composite aerogels is shown in **Figure 1a**. The BNNS was first exfoliated using the urea-assisted balling milling to yield amino-functionalized BNNS. The functionalized BNNS was then used in preparing BNNS/PVA composite aerogels in a UFC process. Hexagonal boron nitride (*h*-BN) (99.5 %, 325 mesh supplied by Alfa Aesar) was exfoliated to obtain BNNS by urea-assisted ball milling at an *h*-BN to urea weight ratio of 1:60 at

400 rpm for 24 h on a planetary ball mill [43]. The ball-milled powders were dispersed in deionized (DI) water by centrifugation at 1000 rpm for 20 min to collect the supernatant, which was washed with DI water four times at 12000 rpm to remove the residual urea and then freeze-dried to obtain 2D BNNSs. The application of urea was proven to be effective in assisting exfoliation while protecting the BNNS from excessive mechanical damage to their lattice structure [22]. The PVA is chosen as the matrix because it is a water-soluble polymer and therefore can be easily tailored into aligned structures using the freeze-casting process. Water-soluble PVA can also enhance the dispersion of BNNS in the aqueous solution, an essential prerequisite for the formation of well-aligned structures during freeze-casting [29]. Moreover, the white color of PVA is beneficial to the solar reflectance of the composite aerogel. The BNNS/PVA composite aerogels were prepared by a UFC process. Freeze-casting is a versatile approach for creating porous structures in materials by controlling the freezing parameters [44]. The process is environmentally friendly as no harmful gases are involved compared to supercritical drying [45]. PVA with a molecular weight ranging 85,000 – 124,000 (supplied by Sigma Aldrich) was dissolved in hot water at 90 °C to prepare two different concentrations of 20 and 50 mg/mL. BNNSs of pre-determined wt% were added to the PVA concentration and stirred for 4 hr and the mixture was poured into a Teflon mold for freeze casting. Liquid nitrogen (LN) was used as coolant to create a large temperature gradient, thereby inducing a high freezing rate which is necessary to achieve small pore sizes. Upon the introduction of LN, ice nuclei developed near the cold source grew horizontally towards the end of the suspension in the Teflon mold, expelling the dispersion of BNNS and PVA into the inter-lamellae among the growing ice fronts. When the freezing process was completed, the sample was transferred into a freeze-dryer maintained at a pressure below 3 Pa to sublimate the ice, forming a highly anisotropic cellular pores structure. The designations of aerogels prepared using different compositions with their physical properties are shown in Table 1.

Table 1. PVA and BNNS loadings and physical properties of different BNNS/PVA composite aerogels.

Designations	PVA Concentration (mg/mL)	BNNS loading (wt%)	Density (mg/cm^3)	Porosity (%)
P20	20	0	31.7 ± 0.34	97.3 ± 0.08
P20/B10		10	22.3 ± 0.38	98.2 ± 0.08
P20/B20		20	29.2 ± 0.36	97.7 + 0.08
P50	50	0	93.3 ± 0.21	92.2 ± 0.05
P50/B5		5	95.5 ± 0.22	92.2 ± 0.05
P50/B10		10	97.0 ± 0.24	92.2 ± 0.05

2.2 Characterization and Measurements

The apparent density (ρ) of the composite aerogel was measured using the mass and volume of three aerogel samples while the skeletal density (ρ_0) was estimated using the weighted density averages of PVA and BNNS. The porosity was determined by Equation (1) [46]:

$$P = \left(1 - \frac{\rho}{\rho_0}\right) \times 100\% \quad (1)$$

The morphologies of the composite aerogel were examined on a scanning electron microscope (SEM, model TM3030) at an accelerating voltage of 15 kV. The exfoliation of BNNSs was confirmed using the Raman spectroscopy (RamanMicro300, Perkin Elmer) and the chemical compositions of *h*-BN and BNNSs were examined using the Fourier transform infrared spectroscopy (FTIR, Bruker Vertex 70 Hyperion 1000) over wavenumbers of 400 – 4000 cm^{-1}. The lateral size and thickness of the BNNS were examined using the atomic force microscopy (AFM, Dimension Icon) while the crystal structure was analyzed through X-ray diffraction (XRD, X'pert Pro). Their thermal properties were determined using a thermal constant analyzer (TPS 2500S, Hot Disk) at room temperature based on the transient plane source method [29,30]. A measuring probe of radius 6.4 mm was sandwiched between two identical samples at an output power of 20 mW and a measuring time of 4 s. Four samples were tested for each composition. The thermographic images of the composite aerogel and commercial insulating foams placed on a hot stage were taken using an infrared (IR) thermal camera (Fluke Ti25). Their mechanical properties

were measured under uniaxial compression on a universal testing machine (MTS 858) in accordance with the specification, ASTM-C165-07, at across head speed of 2 mm/min. The reflectance over the wavelength of 0.3 – 2.5 μm was measured using an ultraviolet-visible-near infrared (UV-*vis*-NIR) spectrometer (Perkin Elmer lambda 950). The emissivity was evaluated from the transmittance measured using FTIR. An IR lamp with a maximum power of 275 W and a wavelength ranging 760 nm – 1 mm was used to simulate thermal irradiance and the intensity was measured using a datalogging solar power meter (TES 1333R).

3. Results and Discussion

3.1 Design and Fabrication of BNNS/PVA Composite Aerogels

The composite aerogels were fabricated using the UFC process (**Figure 1**a, see Section 2.1 for details). The composite aerogel is white in color and of very light weight, as shown in Figure 1b. The SEM images of the composite aerogel present a highly anisotropic structure containing aligned BNNS/PVA cell walls in the axial direction, as shown in Figure 1c, which support the open pore channels with varying diameters, as shown Figure 1d. The anisotropic structure of the composite aerogel is a reflection of the growth of the ice crystals during the UFC process. At the onset of solidification of the colloidal suspension, the nucleation and growth of ice crystals expelled the mixture of BNNS and PVA to form composite lamellar walls between the growing ice fronts. During the freeze-drying process, the ice crystal sublimated leaving behind an open pore structure supported by PVA lamellar cell walls containing BNNS reinforcements.

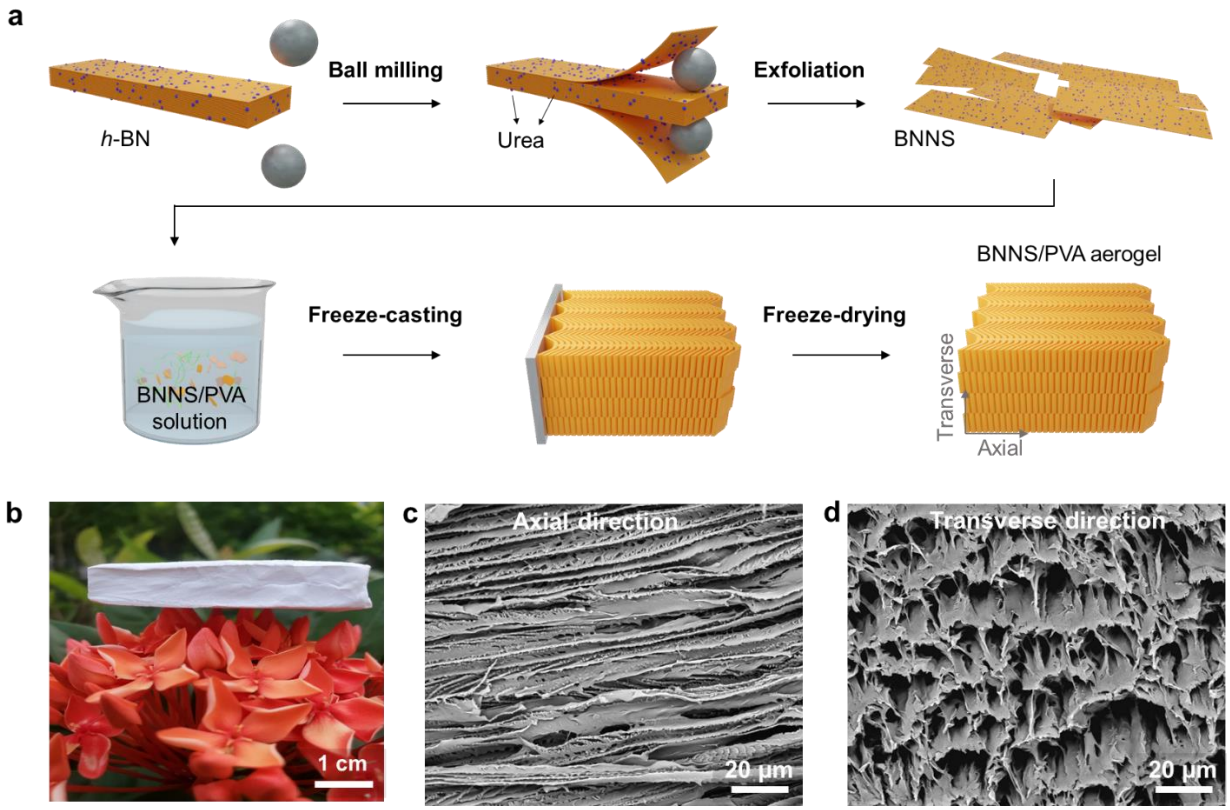

Figure 1. Fabrication and morphologies of BNNS/PVA composite aerogels. (a) Schematic diagram showing the fabrication of composite aerogels with aligned pores by UFC; (b) digital image showing the light weight and white color of the composite aerogel; SEM images showing microstructures of the composite aerogel taken from the (c) axial and (d) transverse cross-sections.

3.2 Morphologies of BNNS and BNNS/PVA Composite Aerogels

The schematics of urea-assisted balling milling for the exfoliation of *h*-BN at atomic scale are shown in Figure S1 and the SEM of BNNS thereby produced is shown in **Figure 2**a, presenting relatively uniform lateral sizes. The AFM images of a few BNNS are shown in Figure 2b and their corresponding height profiles in Figure 2c to reveal the thickness of BNNS ranged 5 – 14 nm while the lateral length ranged from 400 to 973 nm. Given the apparent thickness of 0.9 to 1 nm for a monolayer BN sheet measured by AFM [47], the number of layers was estimated to be from 5 to 14 layers. The large variation in lateral size and thickness of BNNS (Figure 2b-c) could be attributed to the intrinsic size and thickness distribution of *h*-BN precursors as well as the random collision between the balls and the *h*-BN during ball milling [22,48]. The *h*-BN and exfoliated BNNS were examined on a Raman spectrometer, as shown in Figure 2d. There was a shift in the

Raman peak from 1364 to 1366 cm^{-1} after exfoliation, which corresponds to the E_{2g} mode vibration due to successful exfoliation of bulk *h*-BN into few-layer nanosheets [48]. The FTIR spectra shown in Figure 2e showed that there were two characteristic peaks at 763 and 1313 cm^{-1} for *h*-BN corresponding to out-of-plane B-N-B bending vibration and in-plane B-N stretching vibration, respectively. These peaks were also observed in BNNS, indicating preserved B-N-B vibrational modes. In addition, two other peaks were observed at around 1677 and 3340 cm^{-1} attributed to the presence of NH_2 groups. The hydrophilic amino group enhanced the dispersion of BNNS in both DI water and PVA precursor as evidenced by the Tyndall effect observed in BNNS dispersions, see Figure S1. The XRD patterns of bulk *h*-BN and BNNS in Figure 2f showed two noticeable peaks at 26.8°and 55.3° corresponding to the (002) and (004) planes, respectively. Compared to the *h*-BN counterpart, the (002) peak of BNNS presented a significantly reduced intensity and a slightly broadened width, a reflection of thin BN sheets [22]. Other peaks were found at 41.8°, 43.9° and 50.3° corresponding to the (100), (101) and (102) planes which are of lower intensities than in the bulk *h*-BN.

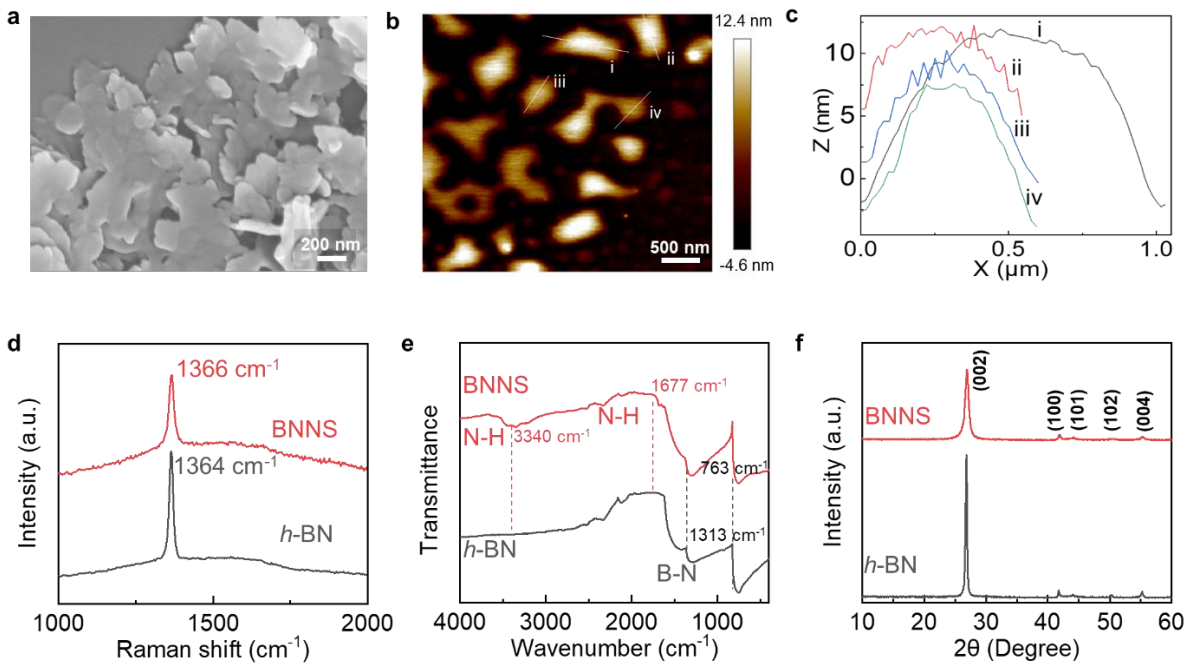

Figure 2. Morphology and chemical composition of BNNS. (a) SEM and (b) AFM images of BNNS; (c) height profiles of BNNS obtained from the AFM; (d) Raman, (e) FTIR, and (f) XRD spectra of bulk *h*-BN and BNNS.

The SEM images of the composite aerogels prepared with different loadings of PVA and BNNS in both the transverse and axial directions are shown in Figure 3 and Figure S2. The SEM images in the transverse direction (Figure 3a-c, S2a-c) show the pore sizes of the composite aerogels, which were formed by sublimation of ice crystals squeezed among the walls of solid solution during the freeze-casting process. The composite aerogel prepared with 20 mg/mL PVA possessed abundant pores with large sizes (Figure 3b) which resembled a honeycomb structure while those prepared with 50 mg/mL PVA looked more like a cellular structure consisting of a number of smaller pores (Figure 3a). The pore sizes of the former aerogel ranged from 20 to 75 μm in diameter much larger than the later counterpart made from 50mg/mL PVA because of the lower solid content in the former. Further, the incorporation of BNNS led to larger pores with lower densities in the P20/B10 (Figure S2c) and P20/B20 (Figure 3c) composite aerogels than P20 acting alone. The lower densities in the composite aerogels than the PVA counterpart (Table 1) may be attributed to the less shrinkage during freeze-drying thanks to the rigid BNNS fillers, which improved the overall mechanical robustness of the aerogel structure [29]. These pores are tens of microns in size, which are too small for air convection to take place within the composite aerogel, a beneficial feature towards achieving thermal insulation. The SEM images of the aerogels taken in the axial direction are shown in Figure 3d-f and Figure S2d – f). The images represent highly aligned multi-layered strands of palm tree leaf-like structure, whose thickness tended to reduce with decreasing solid concentration. The aligned multilayer structure can help dissipate the heat mainly in the axial direction while maintaining thermal insulation in the transverse direction, and provides mechanical support to the composite aerogel. The FTIR spectra shown in Figure S3 include several prominent peaks for PVA: at 3280 cm^{-1} corresponding to the O-H stretching vibration; at 2922 cm^{-1} corresponding to C-H asymmetric stretching vibration; at 1677 cm^{-1} corresponding to the C=O stretching; at 1423 cm^{-1} corresponding to the C-H bending vibration of CH_2; at 1338 cm^{-1} corresponding to the C-H deformation vibration; at 1093 cm^{-1} corresponding to C-O stretching of acetyl groups; and at 830 cm^{-1} corresponding to the C-C stretching vibration. The BNNS/PVA aerogel maintained pretty much similar peaks with an additional peak at 1384 cm^{-1} corresponding to the B-N stretching, evidence of the presence of B-N in the aerogel.

The mechanical properties of the composite aerogels were also examined. Sufficient mechanical properties are an important criterion for the selection of thermally insulating materials. Compressive tests were carried out in both the axial and transverse directions of different

composite aerogels up to a strain of 60 %. Their stress-strain curves and the compressive moduli measured from the initial slopes of the stress-strain curves are shown in **Figure 4**. The compressive moduli of aerogels increased significantly with increasing BNNS loading, which is attributed to the improved bending stiffness of the cell walls with the addition of BNNS [24,29]. The composite aerogels made from 50 mg/mL PVA showed much higher compressive moduli than their counterparts prepared with 20 mg/mL PVA because of the significantly higher densities of the P50-series aerogels than P20-series ones (Table 1). In addition, their axial moduli were three to five times higher than those measured in the transverse direction thanks to the aligned cell walls. The BNNS/PVA aerogels also possessed higher compressive strengths than commercial closed cell foams with compressive strengths ranging 55 – 124 kPa [49], demonstrating the potential of composite aerogels for practical applications.

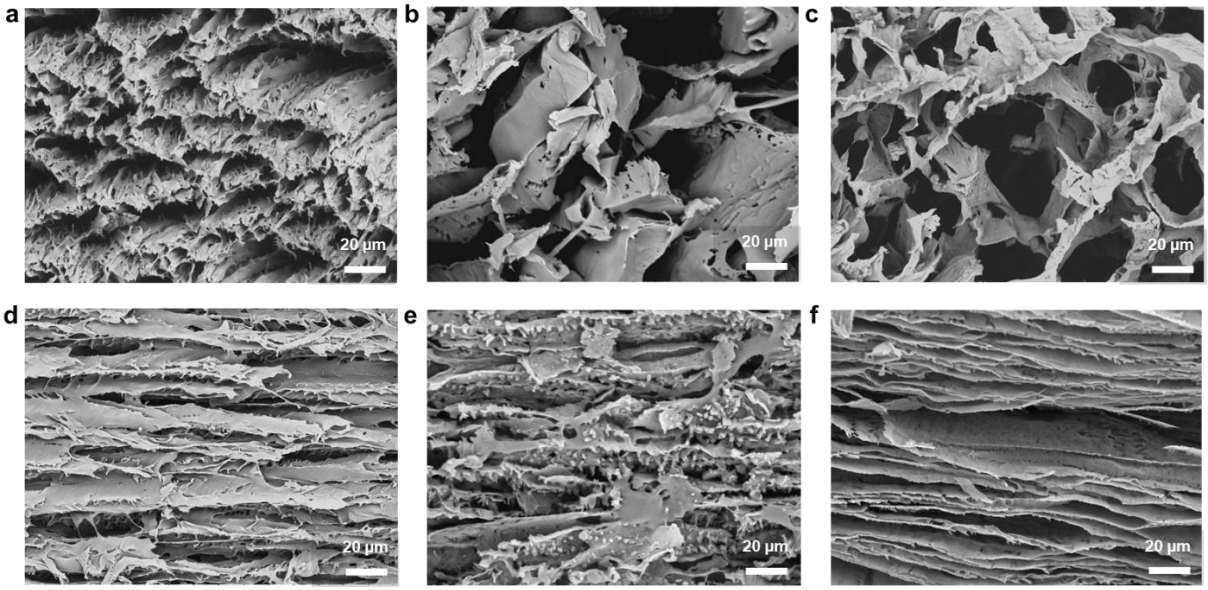

Figure 3. Microstructures of BNNS/PVA aerogel. SEM images of composite aerogel (a,d) P50, (b, e) P20 and (c, f) P20/B20 taken in the (a-c) transverse and (d-f) axial directions.

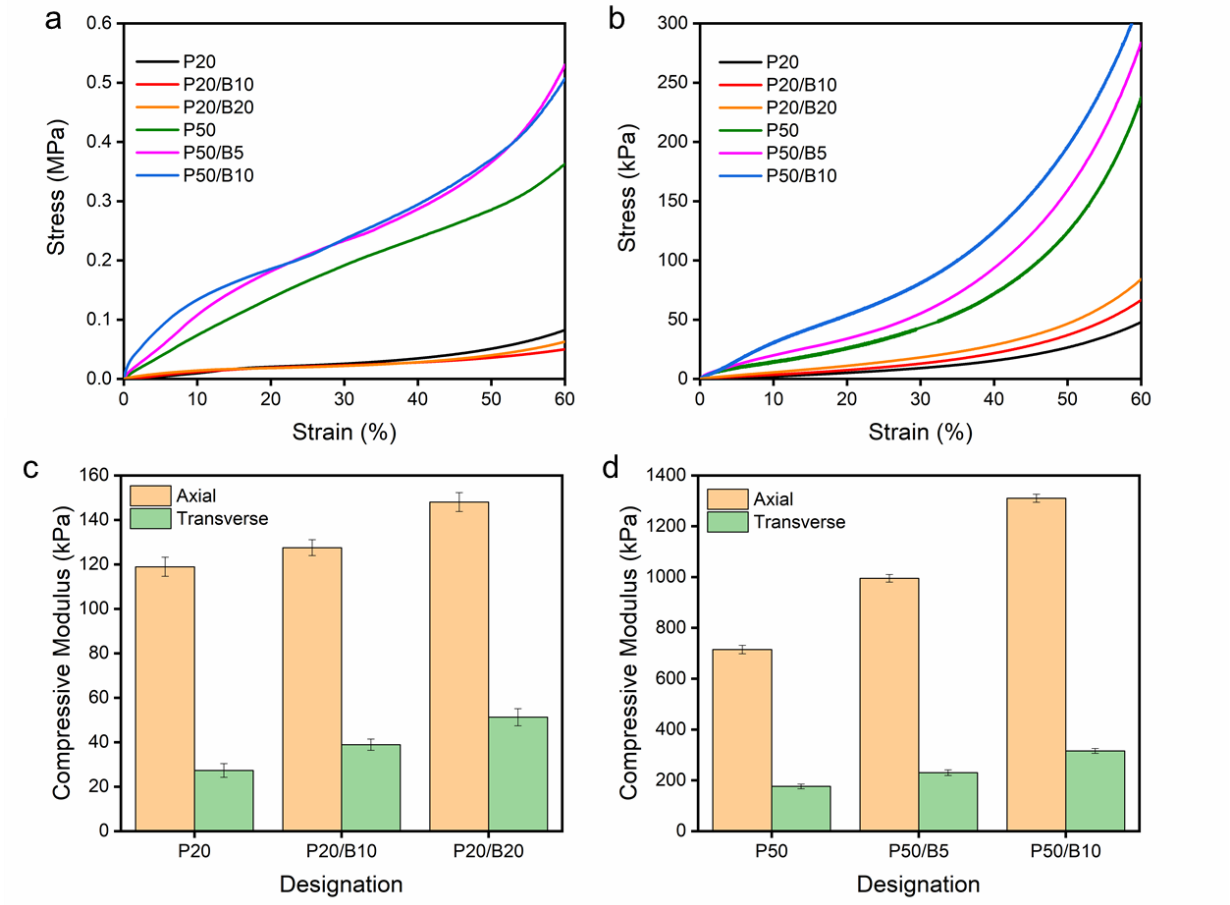

Figure 4. Mechanical properties of composite aerogels. Stress-strain curves measured in the (a) axial and (b) transverse directions. Compressive moduli of composite aerogels prepared with PVA concentrations of (c) 20 and (d) 50 mg/mL.

3.3 Anisotropic Thermal Conductivities of Composite Aerogels

The TCs of composite aerogels with different compositions were measured in two orthogonal directions as shown in **Figure** 5a. Regardless of the composition, the TCs exhibited significant anisotropy with much higher values in the axial than transverse directions due to the highly anisotropic porous structure. Interestingly, the TCs responded differently in the two orthogonal directions with the addition of BNNS. The increasing loading of BNNS in the aligned cell walls gave rise to higher axial TCs for both P20- and P50-series aerogels. It should be noted that the aerogels prepared with 20 mg/mL PVA generally had much lower densities (22 – 32 vs 93 – 97

mg/cm^3) with higher porosities (98 vs 92 %) than those prepared with 50 mg/mL PVA, as shown in Table 1. The reduction in the solid concentration offers room for ice growing fronts to develop into large ice crystals, giving rise to large pores upon sublimation. It is important to mention that their pore sizes (20 – 75 μm) were not large enough to support gas convection but significantly contributed to the porosity of the aerogel. The denser solid networks in P50 imparted higher solid conduction than in P20, resulting in generally higher axial TCs in the former. Interestingly, the TCs in the transverse direction of composite aerogels prepared with 20 mg/mL PVA exhibited significant drops with the addition of BNNS, while those of the aerogels prepared with 50 mg/mL PVA remained largely unchanged with the addition of BNNS. The lower TC of composite aerogel prepared by 20 mg/mL PVA can be associated with the functionally similar variation in density as shown in Figure 5b, which is inversely proportional to the porosity and pore size of the composite aerogel. The addition of rigid BNNS created lower shrinkage in the P20/B10 aerogel than in P20 (Figure S4), giving rise to a larger pore size and higher porosity in the former. The higher porosity meant more air in the aerogel, interrupting phonon transport and thereby contributing to a lower TC of the composite aerogel. The high porosity resulted in an ultralow TC of 20.3 mW/mK at a BNNS content of 10 wt% in P20/B10, which is 15 % lower than that of air (24 mW/m K, dash line in Figure 5a) and ~34 % lower than the aerogel prepared with 50 mg/mL PVA and an equivalent BNNS content. Further raising the BNNS loading to 20 wt% instead increased the density of the composite aerogel, likely because the high density of BNNS outweighed the reduced shrinkage.

The TCAR in general increased with increasing BNNS due to the orientation of BNNS in the aerogel alignment direction, as shown in Figure S5a. It appears that the increase in TCAR is mainly attributed by the increase in TC_L rather than the reduction in $TC_\perp$. A high TCAR is preferred because composites with a high TCAR tend to show better insulating performance as it will also enhance heat movement in the axial direction thereby ensuing thermal insulation in the transverse direction [30]. The hierarchical alignment of BNNS at both micro- and nanoscale made the TC_L increased with increasing BNNS content, as shown in Figure S5b. The aligned cell walls served as better heat conduction paths while the presence of conductive BNNS in the cell wall also contributed to the high TC_L, whose combined effect effectively removed the heat from the composite. Meanwhile, the abundant aligned open pores gave rise to much lower transverse TCs than the axial counterpart. Figure 5c shows a schematic illustration of the microstructural features of the aerogel with effective thermal conduction along the cell walls in the axial direction and

much lower conduction transverse to it. There are four major conduction mechanisms in an open channel, namely solid conduction, gas conduction, gas convection, and radiation. As mentioned earlier, the convection of air in the isolated pore channels was rather difficult because the pore sizes observed in this work appeared to be below 1 mm which is the required pore size for gas convection to occur [50,51]. The TC due to radiation is dependent on the density of materials and temperature [52]. The composite aerogels were of low density and the TC was measured at room temperature. Thus, it can be said that the contribution from radiation to the TC of the aerogels is negligible. Therefore, the conduction plays a major role in determining the TCs in the two directions. The solid conduction is a dominant source of conduction along the axial direction, which accounts for the increased TC with increasing density and BNNS loading. The high TC in the axial direction is vital for heat dissipation. On the contrary, the solid conduction in the transverse direction is greatly suppressed because of the tortuous conduction path and the low TCs of BNNS in the thickness direction, contributing to the low TCs in the transverse direction. Overall, the anisotropic thermal conductivities of aerogel can prevent heat localization in the alignment direction while superinsulation was possible in the transverse direction for effective thermal management [11].

Given the extremely low TC of the P20/B10 composite aerogel in the transverse direction, we have chosen it for further study of its thermal insulation performance, which was compared with commercially available EPS and PU foams. Samples of 2.0 cm in height and 7.5 cm^2 in contact area were placed on a hot plate at 110 °C for 10 min and the IR thermal images were monitored, as shown in Figure 5d. The thermal images revealed that the heat propagation in the composite aerogel was slower than in the EPS foam. Furthermore, the physical structure of EPS foam was broken down after 1 min leading to visible softening along with reduced height after 5 min. In contrast, no significant reduction in height nor softening occurred in the composite aerogel even after 10 min. The thermal insulating performance of PU foam was even worse, showing the onset of melting after 1 min, as shown in Figure S6. The above observation suggests that the thermal stability of composite aerogel was significantly enhanced by the introduction of BNNS with a high melting point of ~ 3000 °C despite the relatively inferior thermal stability of the PVA matrix. Also, the thermal insulation performance of the composite aerogel and commercial EPS was quantitatively evaluated by monitoring their top surface temperatures, as shown in Figure 5e. The temperature evolution clearly indicates that the composite aerogel outperformed the commercial

foam in terms of both the time to reach saturation and the saturated temperature. It took about 12 min for the composite aerogel to reach a saturated temperature of 47 ˚C while the EPS foam attained a saturated temperature of 60 ˚C in 3 min. The much lower saturation temperature can be a driving force for potential application of the composite aerogel as superinsulating building envelope.

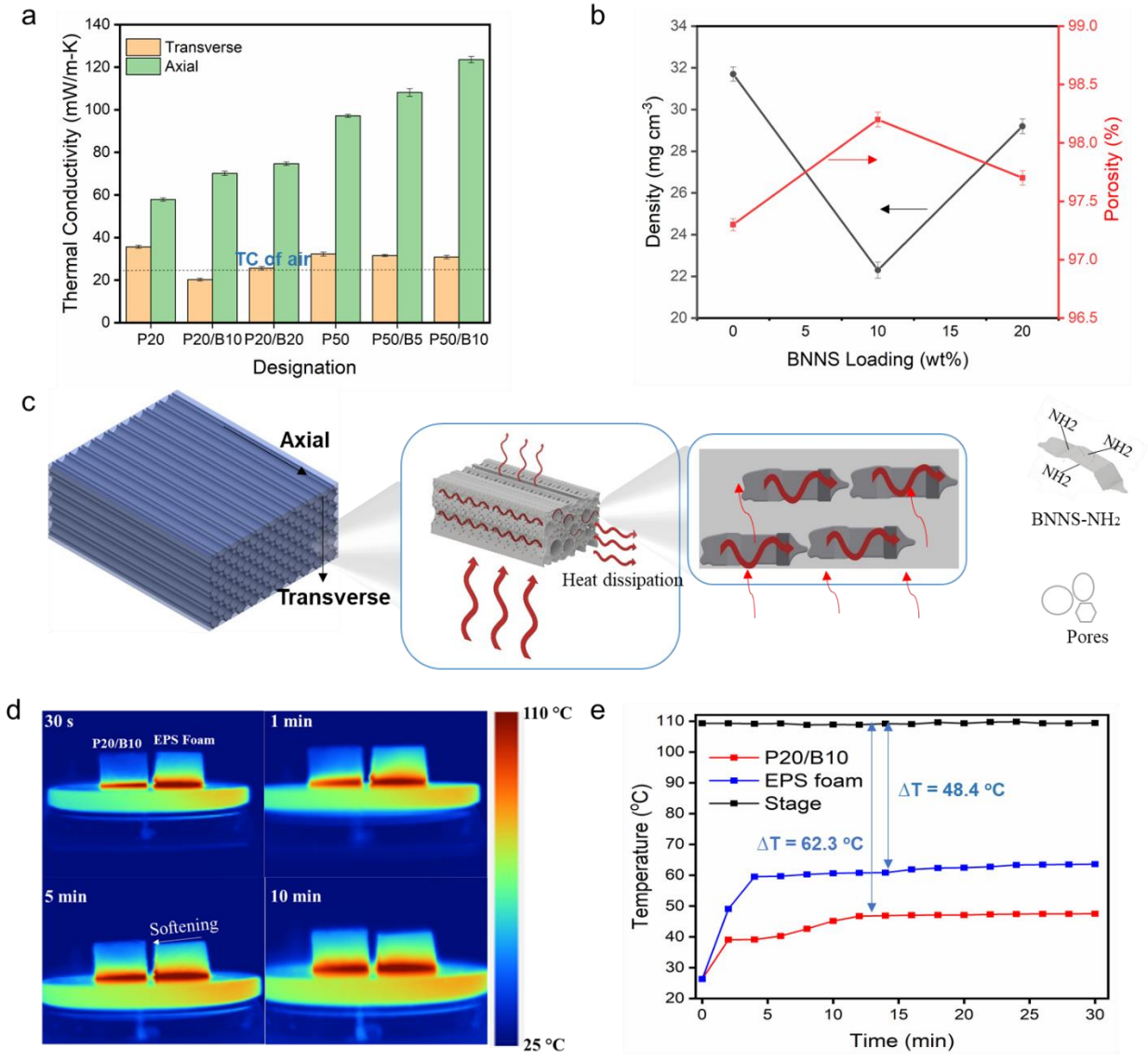

Figure 5. Thermal insulation of composite aerogels. (a) TC of composite aerogels measured in the axial and transverse directions; (b) Densities and porosities of aerogels prepared with 20 mg/mL PVA concentration with different BNNS loadings; (c) Schematic diagram of heat dissipation within the composite aerogel structure; (d) IR thermal images of P20/B10 composite aerogel and

commercial EPS foam taken at different times; (e) Top surface temperatures of P20/B10 composite aerogel and commercial EPS foam recorded at regular intervals when placed on a hot plate at 110 °C.

3.4 Solar Reflectance and Thermal Emittance

The solar reflectance was measured using a UV-*vis*-NIR spectrometer and the solar-intensity weighted reflectance, $\overline{R}_{sun}$, was calculated using Equation 2:

$$\overline{R}_{sun} = \frac{\int_{\lambda_1}^{\lambda_2} I_{sun}(\lambda) R_{sun}(\lambda) d\lambda}{\int_{\lambda_1}^{\lambda_2} I_{sun}(\lambda) d\lambda} \quad (2)$$

where $\overline{R}_{sun}(\lambda)$ is the surface spectral reflectance of samples in the wavelength ranging from $\lambda_1 =$ 0.3 to $\lambda_2 = 2.5$ μm, and $I_{sun}(\lambda)$ is the normalized ASTM G173 solar intensity spectrum. Both the optical reflectance variations in the full solar wavelength ranging from 0.3 to 2.5 μm and the emittance in the atmospheric transparency window ranging from 8 to 13 μm of the P20/B10 composite aerogel, EPS foam and PU foam are shown in **Figure 6a**. The P20/B10 composite aerogel possessed much better solar reflectance than the EPS and PU foams over the whole solar wavelength, exhibiting a solar weighted reflectance of 95 %, 31 % and 93 % higher than the other two materials (Figure S7), respectively. Figure S8 shows the optical reflectance and emittance of other composites aerogels. All composite aerogels exhibited high solar weighted reflectances of over 94% in the solar spectrum. The excellent solar weighted reflectance of the composite aerogel arose from the following mechanisms. First, BNNS and PVA had intrinsic low absorption in the visible spectrum as attested by their white appearance, contributing to the solar reflectance in the visible wavelengths from 0.38 to 0.75 μm. Second, the high porosities of composite aerogels meant abundant pores for the refraction of incident light at solid cell wall/air interfaces because of their largely different refractive indices [29,30,36]. The numerous interfaces enabled multiple reflection of incident light to achieve a high solar reflectance. Third, the BNNS/PVA interfaces also acted as scattering centers thanks to the high contrast between the refractive indices of BNNS (~ 2.1) and PVA (~ 1.5) [33], further enhancing the solar reflectance of composite aerogels. To evaluate the net effect of BNNS on optical properties, PVA and 10 wt% BNNS/PVA composite films without pores were prepared and their solar reflectances were also measured, as shown in Figure S9. The

solar weighted reflectance of the BNNS/PVA film was 4.6 times higher than the PVA film counterpart. The much higher solar reflectance of the composite film can be attributed to the strong interfacial scattering of incident light at the BNNS/PVA interfaces due to the high contrast between the refractive indices of BNNS (~ 2.1) and PVA (~ 1.5) [41]. Based on this observation, it can be said that the incident rays passing through the highly porous microstructure of composite aerogels were refracted at both the air/solid and BNNS/PVA interfaces [30], resulting in multiple scattering to send the radiation back to the surface for much improved reflectance in the composite aerogel. The high optical reflectance of composite aerogels mitigated the solar heat transmission and absorption during daytime, eliminating the need for additional reflective coatings.

The thermal emittance of the composite aerogel, ε, was evaluated using Equation 3:

$$\varepsilon = 1 - R - T \quad (3)$$

where R and T are the reflectance and transmittance, respectively. Figure 6a presents the P20/B 10 composite aerogel had a high emittance of ~ 93 % in the atmospheric transparency window ranging from 8 to 13 μm, higher than both commercial insulating EPS and PU foams. The neat P20 and P50 aerogels without BNNS fillers exhibited slightly higher emittances of 94.8 % than the composite aerogels (Figure S8). This means that the high emittance mainly arose from the highly emissive hydroxyl groups in PVA rather than BNNS, which had few functional groups to facilitate thermal emission. The hydroxyl groups contributed to the IR absorption because of the stretching and bending of O-H, C-O, and C-C bonds, as evidenced by the absorption peaks in the IR wavelengths (Figure S3), which was responsible for the high emittance of PVA. Overall, the high heat emittance means the radiation of the absorbed heat to the cold outer space through the atmosphere transparent window during daytime without consuming extra energy [53].

The optical and thermal properties of the composite aerogel are compared with state-of-the-art thermally insulating materials and high reflectance composite aerogels, as shown in Figure 6b. It is clearly seen that our composite aerogel outperformed the majority of existing materials in terms of both reflectance and TC, with the exception of thermal insulating cooler (TIC) [54] which had a marginally lower TC yet a lower reflectance and PE aerogel [55] having a higher reflectance with a much higher TC of 28 mW/mK. Further, our composite aerogel possessed a lower density of 22.3 mg/cm^3 which is about 79 % lower than the TIC counterpart of 108 mg/cm^3. Thus, it can be said that the BNNS/PVA composite aerogel delivered an optimal combination of desirable

functional properties required for building thermal management among the materials studied thus far.

It was demonstrated [38,56] that the materials required for effective passive cooling must have (i) a high sunlight reflectance in order to minimize the incident solar heat absorbed by the structure, (ii) a high LWIR emittance to radiate absorbed heat in the structure to the cold outer space through the atmospheric transparency window, and (iii) a low TC to mitigate the parasitic heat gain from the surrounding environment. For practical cooling application of thermal insulation and selective optical reflection/emission capabilities, the composite aerogel was subjected to simulated light irradiance of 1175 ± 6 W/m^2 which is similar to the sunlight intensity reaching the earth surface (1000 W/m^2) for 100 min along with other materials, including EPS foam and glass. The experimental setup is schematically presented in Figure S10 where a cubic chamber of 40 mm x 40 mm x 30 mm was constructed using EPS foam and sealed with aluminum foil to minimize solar absorption. The top windows of the cubic chambers were covered with three different materials with a thickness of 5 mm and the internal temperatures were monitored. The temperature reached saturation points of 61.0 and 49.2 °C when the top surface was covered with glass and EPS foam, respectively, as shown in Figure 6c. These values are about 64 % and 32 % higher than the composite aerogel counterpart. The composite aerogel maintained a constant temperature of 37.1 ± 0.3 °C which is close to the normal human body temperature of 37.2°C. The excellent thermal management capability of composite aerogel to maintain indoor thermal comfort stemmed from the unique combination of high sunlight reflectance, anisotropic TCs, and excellent LWIR emittance, as schematically shown in Figure 6d. The incident lights were effectively scattered multiple times both at the BNNS/PVA and pore/solid interfaces thanks to the difference in refractive indices between PVA, BNNS and air [30,33]. The high solar reflectance in the UV region (0.3 to 0.4 μm, Figure 6a) has an added advantage of minimizing the absorption of harmful UV rays, which can cause discoloration, fading, cracking, and warping of polymeric aerogels. The reduced amount of absorbed UV radiation is beneficial to a longer service life of the aerogel. Further, it eliminates the need for additional reflectance coatings, a common design requirement used in thermal insulation materials. Moreover, the highly anisotropic TC allows the heat to dissipate horizontally while preventing conduction in the thickness direction, so that the heat gained from the external environment can be mitigated. In addition, the abundant functional groups in PVA impart a high LWIR emittance, facilitating the passive cooling by radiation through the

atmospheric transparency window. All the above ameliorating functional and structural features enabled the composite aerogel to maintain a temperature lower than other insulating materials. These excellent attributes make the BNNS composite aerogel a potential candidate for interior thermal cooling by reflecting sunlight and dissipating heat into the atmosphere.

To further probe the practical energy saving potential of the composite aerogel, we compared the annual energy consumption for maintaining an indoor temperature of 26 ℃ in a building with and without composite aerogel using EnergyPlus (details in Note 1, Supplementary Information). The energies consumed for cooling the building model in twelve cities and the resulting cooling energy savings are shown in Figure 6e and f, respectively. When the P20/B10 composite aerogel was used as the building envelope, a significant reduction of ~ 50 % on average across different cities in the energy required for indoor cooling was achieved thanks to its aforementioned outstanding thermo-optical insulating properties. Indeed, this finding demonstrates the potential of our composite aerogel as a superinsulating building envelope for significantly reduced energy consumption towards carbon neutrality.

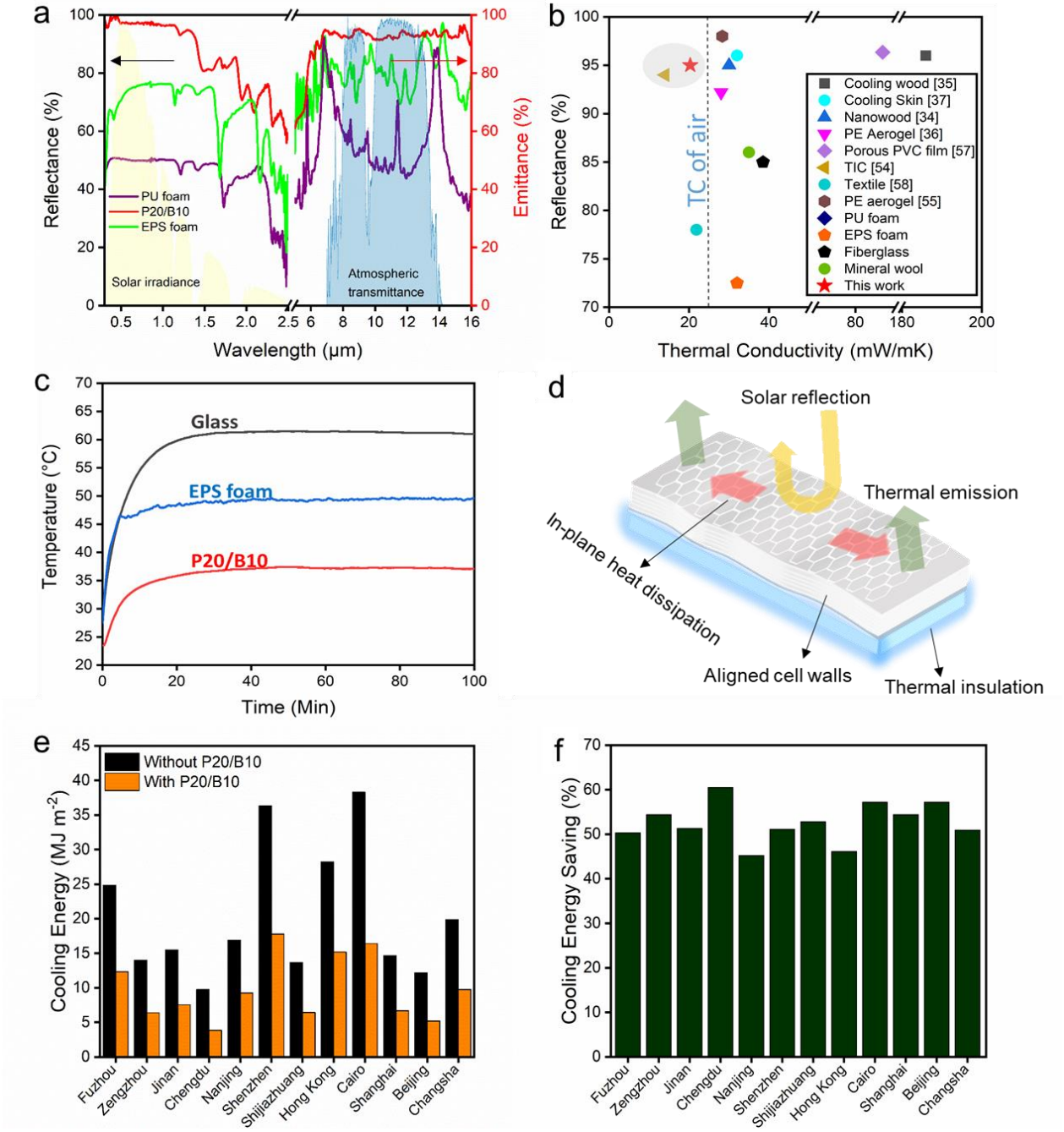

Figure 6. Optical and thermal performance of composite aerogel. (a) Reflectance and emittance spectra of P20/B10, EPS and PU foam; (b) comparison of reflectance and TC of the current composite aerogel with state-of-the-art thermally insulating materials; (c) temperature evolution inside the chambers covered with P20/B10 composite aerogel, glass plate and EPS foam; (d) schematic illustration of optical and thermal management mechanisms of composite aerogels during daytime; (e) simulated year-round cooling energy consumptions in twelve cities with and

without P20/B10 as the building envelope; and (f) percentage of cooling energy saved when P20/B10 was used as the building envelope.

4. Conclusion

Anisotropic and lightweight BNNS/PVA composite aerogels have been developed using the UFC technique. Benefitting from the highly aligned porous channels, the composite aerogel with an optimal BNNS content, P20/B10, exhibited an ultralow TC of 20.3 mW/mK in the transverse direction. The anisotropic structure and the presence of BNNSs in the cell wall enabled the composite aerogel to dissipate heat in the alignment direction while maintain thermal insulation transverse to it. The composite aerogel delivered better thermal insulation by about 20 % than commercial EPS and PU foams. The highly porous cell walls also endowed the aerogel with an excellent solar-weighted reflectance of 95.0 % in the solar wavelength of 0.3 – 2.5 μm and a high emittance of 93 % within the atmospheric transparency window. These exceptional optical capabilities of the composite aerogel facilitated low heat absorption under high solar irradiance and high thermal emittance to environment during daytime, thereby reducing the amount of energy required to maintain indoor thermal comfort. These desired characteristics make the composite aerogels promising material for thermal management in buildings and thermo-protective covers, demonstrating significant energy saving as a superinsulating building envelope towards reduction of carbon emission.

Acknowledgements: This work was financially supported by the Hong Kong PhD Fellowship Scheme (HKPFS) and Research Grants Council (GRF Projects: 16205517, 16209917 and 16200720) and Innovation and Technology Commission (ITS/012/19) of Hong Kong SAR. This project was also supported by the Research Institute for Sports Science and Technology of PolyU (P0043535) and start-up fund for new recruits of PolyU (Nos. P0038855 and P0038858). Technical assistance from the Materials Characterization and Preparation Facility (MCPF), the Advanced Engineering Material Facility (AEMF), and the Environmental Central Facility (ENVF) at HKUST is also appreciated.

References

[1] International Energy Agency. Transition to Sustainable Buildings: Strategies and Opportunities to 2050 2013.

[2] Yang L, Yan H, Lam JC. Thermal comfort and building energy consumption implications – A review. Appl Energy 2014;115:164–73.

[3] United States Environment Protection Agency. Phaseout of Ozone-Depleting Substances (ODS) 2018.

[4] King DA. Climate Change Science: Adapt, Mitigate, or Ignore? Science 2004;303:176–7. https://doi.org/10.1126/science.1094329.

[5] Costa A, Keane MM, Torrens JI, Corry E. Building operation and energy performance: Monitoring, analysis and optimisation toolkit. Appl Energy 2013;101:310–6.

[6] International Energy Agency. World Energy Outlook 2006 2006:601.

[7] Global Alliance for Building and Construction. Global Status Report: Towards a Zero-Emission, Efficient and Resilient Buildings and Construction Sector 2018:73.

[8] Jelle BP. Traditional, state-of-the-art and future thermal building insulation materials and solutions – Properties, requirements and possibilities. Energy and Build 2011;43:2549–63.

[9] An L, Petit D, Di Luigi M, Sheng A, Huang Y, Hu Y, et al. Reflective Paint Consisting of Mesoporous Silica Aerogel and Titania Nanoparticles for Thermal Management. ACS Appl Nano Mater 2021;4:6357–63.

[10] Bao H, Yan C, Wang B, Fang X, Zhao CY, Ruan X. Double-layer nanoparticle-based coatings for efficient terrestrial radiative cooling. Sol Energy Mater Sol Cells 2017;168:78–84.

[11] Mandal J, Fu Y, Overvig AC, Jia M, Sun K, Shi NN, et al. Hierarchically porous polymer coatings for highly efficient passive daytime radiative cooling. Science 2018;362:315–9.

[12] Rizvi A, Chu RKM, Park CB. Scalable Fabrication of Thermally Insulating Mechanically Resilient Hierarchically Porous Polymer Foams. ACS Appl Mater Interfaces 2018;10:38410–7.

[13] Krasnovskih MP, Maksimovich NG, Vaisman YaI, Ketov AA. Thermal stability of mineral-wool heat-insulating materials. Russ J Appl Chem 2014;87:1430–4.

[14] Wicklein B, Kocjan A, Salazar-Alvarez G, Carosio F, Camino G, Antonietti M, et al. Thermally insulating and fire-retardant lightweight anisotropic foams based on nanocellulose and graphene oxide. Nat Nanotechnol 2015;10:277–83.

[15] Yuan B, Ding S, Wang D, Wang G, Li H. Heat insulation properties of silica aerogel/glass fiber composites fabricated by press forming. Mater Lett 2012;75:204–6.

[16] Chu S, Majumdar A. Opportunities and challenges for a sustainable energy future. Nature 2012;488:294–303.

[17] Si Y, Wang X, Dou L, Yu J, Ding B. Ultralight and fire-resistant ceramic nanofibrous aerogels with temperature-invariant superelasticity. Sci Adv 2018;4:eaas8925.

[18] Fricke J, Emmerling A. Aerogels. J Am Ceram Soc 1992;75:2027–35.

[19] Su L, Wang H, Niu M, Fan X, Ma M, Shi Z, et al. Ultralight, Recoverable, and High-Temperature-Resistant SiC Nanowire Aerogel. ACS Nano 2018;12:3103–11.

[20] Liang C, Wang Z. Eggplant-derived SiC aerogels with high-performance electromagnetic wave absorption and thermal insulation properties. Chem Eng J 2019;373:598–605.

[21] Zeng X, Ye L, Yu S, Sun R, Xu J, Wong C-P. Facile Preparation of Superelastic and Ultralow Dielectric Boron Nitride Nanosheet Aerogels via Freeze-Casting Process. Chem Mater 2015;27:5849–55.

[22] Lei W, Mochalin VN, Liu D, Qin S, Gogotsi Y, Chen Y. Boron nitride colloidal solutions, ultralight aerogels and freestanding membranes through one-step exfoliation and functionalization. Nat Commun 2015;6:8849.

[23] Li G, Zhu M, Gong W, Du R, Eychmüller A, Li T, et al. Boron Nitride Aerogels with Super- Flexibility Ranging from Liquid Nitrogen Temperature to 1000 °C. Adv Funct Mater 2019;29:1900188.

[24] Xu X, Zhang Q, Hao M, Hu Y, Lin Z, Peng L, et al. Double-negative-index ceramic aerogels for thermal superinsulation. Science 2019;363:723–7.

[25] Shen X, Kim J-K. 3D graphene and boron nitride structures for nanocomposites with tailored thermal conductivities: recent advances and perspectives. Funct Compos Struct 2020;2:022001.

[26] Zhang X, Ni X, Li C, You B, Sun G. Co-gel strategy for preparing hierarchically porous silica/polyimide nanocomposite aerogel with thermal insulation and flame retardancy. J Mater Chem A 2020;8:9701–12.

[27] Jelle BP, Gustavsen A, Baetens R. The path to the high performance thermal building insulation materials and solutions of tomorrow. J Build Phys 2010;34:99–123.

[28] Guo H, Meador MAB, McCorkle L, Quade DJ, Guo J, Hamilton B, et al. Tailoring Properties of Cross-Linked Polyimide Aerogels for Better Moisture Resistance, Flexibility, and Strength. ACS Appl Mater Interfaces 2012;4:5422–9.

[29] Yang J, Chan K-Y, Venkatesan H, Kim E, Adegun MH, Lee J-H, et al. Superinsulating BNNS/PVA Composite Aerogels with High Solar Reflectance for Energy-Efficient Buildings. Nano-Micro Lett 2022;14:54.

[30] Chan K-Y, Shen X, Yang J, Lin K-T, Venkatesan H, Kim E, et al. Scalable anisotropic cooling aerogels by additive freeze-casting. Nat Commun 2022;13:5553.

[31] Qin Y, Peng Q, Zhu Y, Zhao X, Lin Z, He X, et al. Lightweight, mechanically flexible and thermally superinsulating rGO/polyimide nanocomposite foam with an anisotropic microstructure. Nanoscale Adv 2019;1:4895–903.

[32] Song J, Chen C, Yang Z, Kuang Y, Li T, Li Y, et al. Highly Compressible, Anisotropic Aerogel with Aligned Cellulose Nanofibers. ACS Nano 2018;12:140–7.

[33] Li P, Wang A, Fan J, Kang Q, Jiang P, Bao H, et al. Thermo- Optically Designed Scalable Photonic Films with High Thermal Conductivity for Subambient and Above- Ambient Radiative Cooling. Adv Funct Mater 2022;32:2109542.

[34] Li T, Song J, Zhao X, Yang Z, Pastel G, Xu S, et al. Anisotropic, lightweight, strong, and super thermally insulating nanowood with naturally aligned nanocellulose. Sci Adv 2018;4:eaar3724.

[35] Li T, Zhai Y, He S, Gan W, Wei Z, Heidarinejad M, et al. A radiative cooling structural material. Science 2019;364:760–3.

[36] Leroy A, Bhatia B, Kelsall CC, Castillejo-Cuberos A, Di Capua H. M, Zhao L, et al. High-performance subambient radiative cooling enabled by optically selective and thermally insulating polyethylene aerogel. Sci Adv 2019;5:eaat9480.

[37] Yang M, Zou W, Guo J, Qian Z, Luo H, Yang S, et al. Bioinspired "Skin" with Cooperative Thermo-Optical Effect for Daytime Radiative Cooling. ACS Appl Mater Interfaces 2020;12:25286–93.

[38] Raman AP, Anoma MA, Zhu L, Rephaeli E, Fan S. Passive radiative cooling below ambient air temperature under direct sunlight. Nature 2014;515:540–4.

[39] Zhao D, Aili A, Zhai Y, Lu J, Kidd D, Tan G, et al. Subambient Cooling of Water: Toward Real-World Applications of Daytime Radiative Cooling. Joule 2019;3:111–23.

[40] Takahashi S, Imai Y, Kan A, Hotta Y, Ogawa H. Dielectric and thermal properties of isotactic polypropylene/hexagonal boron nitride composites for high-frequency applications. J Alloys Compd 2014;615:141–5.

[41] Rah Y, Jin Y, Kim S, Yu K. Optical analysis of the refractive index and birefringence of hexagonal boron nitride from the visible to near-infrared. Opt Lett 2019;44:3797.

[42] Kusunose T, Uno Y, Tanaka Y, Sekino T. Isotropic enhancement of the thermal conductivity of polymer composites by dispersion of equiaxed polyhedral boron nitride fillers. Compos Sci Technol 2021;208:108770.

[43] Wu Y, Wang Z, Shen X, Liu X, Han NM, Zheng Q, et al. Graphene/Boron Nitride–Polyurethane Microlaminates for Exceptional Dielectric Properties and High Energy Densities. ACS Appl Mater Interfaces 2018;10:26641–52.

[44] Yang J, Shen X, Yang W, Kim J-K. Templating strategies for 3D-structured thermally conductive composites: Recent advances and thermal energy applications. Prog Mater Sci 2023;133:101054.

[45] Shen X, Zheng Q, Kim J-K. Rational design of two-dimensional nanofillers for polymer nanocomposites toward multifunctional applications. Prog Mater Sci 2021;115:100708.

[46] Wu Y, Wang Z, Liu X, Shen X, Zheng Q, Xue Q, et al. Ultralight Graphene Foam/Conductive Polymer Composites for Exceptional Electromagnetic Interference Shielding. ACS Appl Mater Interfaces 2017;9:9059–69.

[47] Griffin A, Harvey A, Cunningham B, Scullion D, Tian T, Shih C-J, et al. Spectroscopic Size and Thickness Metrics for Liquid-Exfoliated *h* -BN. Chem Mater 2018;30:1998–2005.

[48] Guo F, Shen X, Zhou J, Liu D, Zheng Q, Yang J, et al. Highly Thermally Conductive Dielectric Nanocomposites with Synergistic Alignments of Graphene and Boron Nitride Nanosheets. Adv Funct Mater 2020;30:1910826.

[49] Foam types https://foamonline.com/closed-cell-foam/ (accessed December 18, 2022).

[50] Zhao S, Zhang Z, Sèbe G, Wu R, Rivera Virtudazo RV, Tingaut P, et al. Multiscale Assembly of Superinsulating Silica Aerogels Within Silylated Nanocellulosic Scaffolds: Improved Mechanical Properties Promoted by Nanoscale Chemical Compatibilization. Adv Funct Mater 2015;25:2326–34.

[51] Kaganer MG. Thermal insulation in cryogenic engineering. Israel Program for Scientific Translations 1969.

[52] Zhan H-J, Wu K-J, Hu Y-L, Liu J-W, Li H, Guo X, et al. Biomimetic Carbon Tube Aerogel Enables Super-Elasticity and Thermal Insulation. Chem 2019;5:1871–82.

[53] Lin K-T, Han J, Li K, Guo C, Lin H, Jia B. Radiative cooling: Fundamental physics, atmospheric influences, materials and structural engineering, applications and beyond. Nano Energy 2021;80:105517.

[54] Zhong H, Li Y, Zhang P, Gao S, Liu B, Wang Y, et al. Hierarchically Hollow Microfibers as a Scalable and Effective Thermal Insulating Cooler for Buildings. ACS Nano 2021;15:10076–83.

[55] He R, Liao Y, Huang J, Cheng T, Zhang X, Yang P, et al. Radiant air-conditioning with infrared transparent polyethylene aerogel. Mater Today Energy 2021;21:100800.

[56] Feng J, Santamouris M, Shah KW, Ranzi G. Thermal analysis in daytime radiative cooling. IOP Conf Ser: Mater Sci Eng 2019;609:072064.

[57] Tao Y, Mao Z, Yang Z, Zhang J. Preparation and characterization of polymer matrix passive cooling materials with thermal insulation and solar reflection properties based on porous structure. Energy Build 2020;225:110361.

[58] Cui Y, Gong H, Wang Y, Li D, Bai H. A Thermally insulating textile inspired by polar bear hair. Adv Mater 2018;30:1706807.